JOURNAL OF GEOPHYSICAL RESEARCH, VOL. 115, A11311, doi:10.1029/2009JA015236, 2010

OH and OI airglow layer modulation by ducted short-period gravity waves: Effects of trapping altitude

Jonathan B. Snively,[1,2] Victor P. Pasko,[3] and Michael J. Taylor[1]

Received 26 December 2009; revised 22 May 2010; accepted 28 May 2010; published 10 November 2010.

[1] Perturbations to the OH and OI [O(^1S) 557.7 nm] airglow layers by ducted gravity waves near the Brunt-Väisälä period are investigated using a 2-D numerical model. Airglow signatures of these waves are strongly determined by perturbations of O, O_3, and H, which exhibit peak densities near and above mesopause. Strong periodic vertical wind components of short-period gravity waves induce opposite relative density perturbations above and below the layer density peaks. Airglow signatures for ducted waves depend on the specific vertical shapes and altitudes of the wave packets relative to ambient species density profiles; waves perturbing only the bottoms or tops of the layers produce signatures differing from those able to perturb the entire layer thickness. Line-of-sight cancellation occurs between opposite perturbations above and below airglow layer peaks, even for standing waves without vertical phase progression. Integrated brightness-weighted temperature and intensity can thus appear in-phase or antiphase for standing waves, depending on the wave-packet altitude relative to the density gradients. Comparisons of OH and OI layer intensities also reveal in-phase or antiphase relative intensity responses and do not directly indicate the phase of the wave perturbations at layer peak altitudes. Despite this ambiguity, simultaneous brightness-weighted temperature measurements may provide additional insight into wave structure, amplitude, and trapping altitude. For waves of sufficient amplitude that perturb steep density gradients, nonlinearity of the airglow response may be observable; this effect is most prominent when strong cancellation of the linear signature occurs.

Citation: Snively, J. B., V. P. Pasko, and M. J. Taylor (2010), OH and OI airglow layer modulation by ducted short-period gravity waves: Effects of trapping altitude, *J. Geophys. Res.*, *115*, A11311, doi:10.1029/2009JA015236.

1. Introduction

[2] Optical emissions from chemically active airglow layers at mesopause altitudes are readily monitored by ground- and space-based low-light imaging systems [*Taylor*, 1997]. Measurements of perturbations to the airglow layers are now used to observe MLT-region wave phenomena at a broad range of scales, from tides [e.g., *Taylor et al.*, 1999; *Zhang and Shepherd*, 1999; *Zhao et al.*, 2005] to localized instabilities associated with small-scale wave breaking [e.g., *Yamada et al.*, 2001; *Hecht*, 2004; *Li et al.*, 2005]. Image data clearly exhibit gravity wave modulation of emission intensities and temperatures, and long-term observations provide significant insight into the averaged propagation, directionality, and seasonality of small-scale gravity waves [e.g., *Taylor et al.*, 1997; *Walterscheid et al.*, 1999; *Nakamura et al.*, 1999; *Hecht et al.*, 2001; *Chung et al.*, 2003; *Nielsen et al.*, 2006a]. In particular, small-scale and short-period gravity wave propagation ($\lambda_x <$ 40 km, $\tau <$ 10 min) and effects at mesopause altitudes have been studied, discovering abundant thermally and Doppler-ducted waves [e.g., *Hecht et al.*, 2001; *Isler et al.*, 1997], and "mesospheric bores" exhibiting nonlinear ducted wave structure and front-like propagation characteristics [e.g., *Taylor et al.*, 1995; *Smith et al.*, 2003; *Nielsen et al.*, 2006b].

1.1. Short-Period Gravity Waves

[3] Short-period gravity waves are especially able to induce strong modulation of the airglow layers. Large vertical wavelengths of short-period gravity waves reduce cancellation effects within airglow layers [e.g., *Hickey and Yu*, 2005, and references therein], and strong vertical fluid perturbations lead to strong density perturbations [*Tarasick and Shepherd*, 1992], thereby enhancing their visibility to ground-based instruments. These effects are especially prominent for ducted waves that are vertically standing within the airglow region [e.g., *Hines and Tarasick*, 1994; *Snively and Pasko*, 2005; *Snively et al.*, 2007], which may explain the very large number of short-period and small-scale wave signatures observed that are ducted or evanescent [e.g., *Isler et al.*, 1997; *Simkhada et al.*, 2009].

[4] This bias leads to complications when studying gravity wave signatures at periods shorter than several tens of

[1]Center for Atmospheric and Space Sciences, Utah State University, Logan, Utah, USA.
[2]Now at Department of Physical Sciences, Embry-Riddle Aeronautical University, Daytona Beach, Florida, USA.
[3]Communications and Space Sciences Laboratory, Pennsylvania State University, University Park, Pennsylvania, USA.

0148-0227/10/2009JA015236

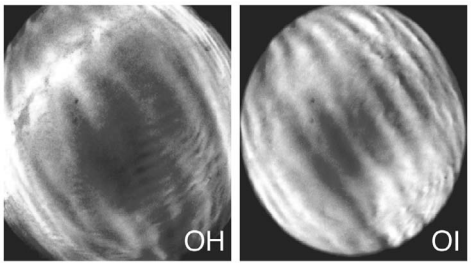

Figure 1. Example all-sky images for OH Meinel band and OI 557.7 nm emissions, showing gravity wave structure at a range of scales. Images are contrast-stretched to reveal details of the wave dynamics.

minutes [e.g., *Swenson et al.*, 2000; *Fritts*, 2000], because Doppler shifts of wave intrinsic frequency lead to variations in vertical wavelength and wave polarization which can significantly influence the resulting airglow signatures. Short-period waves are also prone to refraction for periods approaching the Brunt-Väisälä, and any local region of opposing wind that the wave encounters near mesopause may lead to enhancement of airglow intensity perturbations as the wave vertical wavelength becomes very large. This poses a distinct challenge in estimations of wave momentum flux as, under these circumstances, intensity grows to a relative maximum despite minimal vertical flux of horizontal momentum [*Fritts*, 2000]. Consequently, flux calculations from airglow image data must be limited to larger-scale wave events [*Liu and Swenson*, 2003; *Vargas et al.*, 2007], despite the predominance of shorter-period waves.

[5] Although their role in the MLT momentum budget remains elusive, ducted short-period waves observed in airglow data provide insight into other aspects of atmospheric dynamics. Waves launched by tropospheric sources may directly become ducted at high altitude via upward tunneling [*Fritts and Yuan*, 1989; *Walterscheid et al.*, 2001; *Sutherland and Yewchuk*, 2004; *Yu and Hickey*, 2007] or may excite new ducted waves by various linear and nonlinear processes [*Chimonas et al.*, 1996; *Vadas et al.*, 2003; *Snively and Pasko*, 2008]. Ducted waves may be observed at distances very far from original sources, and they provide lasting signatures of other wave activity [e.g., *Walterscheid et al.*, 1999; *Hecht et al.*, 2001; *Snively and Pasko*, 2003; *Yu and Hickey*, 2007].

[6] Variable atmospheric structure plays a significant role in short-period gravity wave propagation and the characteristics of ducted waves, especially those that are fully ducted, which are strongly governed by the ambient atmospheric wind and temperature profiles. When atmospheric wind and/or temperature profiles are known, via meteor radar and/or lidar data, the characteristics of ducted waves may be estimated and modeled to a relatively high degree of accuracy. Studies of simultaneous airglow image and meteor radar wind data by *Isler et al.* [1997] and *Simkhada et al.* [2009] identified alternating regions of evanescence and propagation throughout mesopause, leading often to one or more candidate duct regions in which short-period waves may become trapped. Simulations reveal strong standing wave structure in the vicinity of the airglow layers for such events [e.g., *Simkhada et al.*, 2009], from which the dominant airglow perturbations likely arose.

[7] Airglow signatures of ducted and standing waves, and their relationships to actual wave dynamics and vertical structure, have been recent topics of controversy. Events characterized as "mesospheric bores" [e.g., *Dewan and Picard*, 1998, 2001] exhibit distinct in-phase or antiphase relationships between airglow emission intensities arising from different layers [e.g., *Taylor et al.*, 1995; *Smith et al.*, 2003], suggesting standing wave structure over a range of altitudes [*Hines and Tarasick*, 1994; *Snively and Pasko*, 2005]. However, the phase and amplitude of the airglow intensity response may not be a reasonable proxy for gravity wave-induced temperature or vertical velocity perturbations, owing to biases imposed by the observed photochemical system [*Hines and Tarasick*, 1994; *Snively and Pasko*, 2005; *Snively et al.*, 2007]. Phase and amplitude of the airglow signature depend on both the characteristics of the wave packet itself and the airglow layer being perturbed. In this paper, we investigate specific effects that contribute to ambiguity in these observed signatures. In particular, we propose that new image data featuring both airglow intensity and brightness-weighted temperature can be used to more accurately assess the amplitude, altitude, and relative phase of gravity wave perturbations. In conjunction with ambient temperature and wind fields, these data can facilitate more realistic reconstructions of observed gravity wave events, providing additional constraints to validate model simulations.

1.2. Airglow Photochemistry

[8] Two strong airglow emissions that are used extensively in studies of gravity waves are the $O(^1S)$ 557.7 nm (OI) green line emission and the OH near-infrared Meinel band system emissions. Both emissions are commonly measured by ground-based imagers, and models for associated airglow photochemistry and imposed gravity wave perturbations exist for each, which are reviewed briefly here. Example all-sky images for these filtered optical emissions, showing clear gravity wave structure, are depicted in Figure 1.

[9] The OI 557.7 nm green line emission is centered around 96 km altitude with ~8 km full width at half maximum and arises from the $O(^1S)$ state of atomic oxygen. The dominant source of $O(^1S)$ in the MLT region is likely a two-stage mechanism[e.g., *Barth*, 1961, 1964; *Bates*, 1988]:

$$O + O + M \rightarrow O_2\left(c^1\Sigma_u^-\right) + M, \quad (1)$$

$$O_2\left(c^1\Sigma_u^-\right) + O \rightarrow O\left(^1S\right) + O_2. \quad (2)$$

[10] Early efforts in photochemical modeling of the OI emission were limited by uncertainty regarding the state of excited O_2, which serves as a precursor to $O(^1S)$, and its associated quenching rates [e.g., *Barth*, 1964]. Later studies of the $O(^1S)$ emission concluded that the precursor was indeed likely to be $O_2(c^1\Sigma_u^-)$ [*Bates*, 1988, and references therein]. Details of the OI emission model used for the studies in this paper are presented in section 2.1.

[11] The OH Meinel band airglow arises from the production of vibrationally excited OH(v) molecules, which emit photons during transitions to lower vibrational states. These vibrational bands consist of many rotational lines which have been characterized and studied extensively in spectroscopic literature [*Chamberlain*, 1961, and references therein]. Intensity of the OH emission layer peaks near ~87 km altitude, with ~8 km full width at half maximum, consistent with the peak of OH(v) density. The principle chemical reactions leading to the production of OH(v) are given by

$$H + O_3 \xrightarrow{v=6-9} OH(v) + O_2, \quad (3)$$

$$O + HO_2 \xrightarrow{v=0-3} OH(v) + O_2. \quad (4)$$

Reaction (3) is generally believed to be the primary reaction relevant to OH(v) production, from which lower vibrational states are excited by downward cascade [*McDade et al.*, 1987; *Adler-Golden*, 1997, and references therein]. Reaction (4) also contributes to the lower vibrational states OH($v \leq 3$) [e.g., *Makhlouf et al.*, 1995]; however, it is not accounted for in the modeling studies presented here that focus on the OH(8,3) band emission [*Adler-Golden*, 1997]. Details of the OH emission model used for the studies in this paper are presented in section 2.2.

1.3. Airglow Response to Gravity Waves

[12] Wave-induced modulation of airglow intensity and brightness-weighted (or rotational) temperature is calculated as the response by a set of photochemical equations to an input gravity wave perturbation. Historically, wave-dynamical effects have been quantified via solutions for Krassovsky's ratio (η), which is a complex quantity relating observed brightness-weighted emission temperature T_I and intensity I perturbations ($\eta = \delta I/\delta T_I$) [*Krassovsky*, 1972]. More recently introduced is the concept of a cancellation factor, which is defined as the ratio of airglow intensity or brightness-weighted temperature perturbation amplitude relative to the actual wave temperature perturbation [e.g., *Swenson and Gardner*, 1998; *Vargas et al.*, 2007]. The cancellation factor was used to estimate actual wave amplitudes from observations, allowing calculation of momentum flux.

[13] In analytical models of wave-induced airglow modulation, it is necessary to reconcile the large relative density perturbations arising along the steep gradients above and below chemical layers. *Hines and Tarasick* [1987] proposed that it is analytically helpful to view the problem as a line-of-sight integration and to treat layer perturbations in a Lagrangian context. Vertical translation of the layer does not necessarily lead to changes of the integrated emission intensity, despite the large percent of perturbations of density (in an Eulerian context) that occur above and below the displaced layer. This requires the assumption that the layer is "thin" relative to the wave packet, such that wave perturbations extend fully throughout the minor species layers rather than being restricted only to the upper (density decreasing with altitude) or lower (density increasing with altitude) halves of the layer. In a numerical approach, such as that developed here, layer perturbations can be calculated directly for arbitrary wave packets and initial chemical states, thus eliminating these analytical challenges and allowing study of waves that only partially extend through the airglow layer regions.

[14] Several comprehensive models of wave interactions with chemistry have been developed. *Walterscheid et al.* [1987] modeled the OH airglow modulation by assuming that emission intensity was proportional to OH production rate, with input perturbations defined by linear equations for gravity wave motion, to find solutions for η. This model was later expanded to allow calculations from an extended emitting layer [*Schubert and Walterscheid*, 1988].

[15] A later comprehensive model for OH airglow modulation was presented by *Makhlouf et al.* [1995]. Using initial minor and major species density profiles given by a steady state model [*Winick*, 1983], OH vibrational state densities for v = 0–9 were obtained from a detailed photochemistry model. This approach allowed calculation of emissions for individual OH(v) bands, where gravity wave effects were incorporated analytically as perturbations to densities and kinetic temperature. *Makhlouf et al.* [1998] later utilized the multiband OH model in comparison studies with a new OI 557.7 nm emission model. Signatures of short-period waves similar to those observed by *Taylor et al.* [1995] were investigated, finding significant variations in phase and intensity responses between the OH and OI layers for waves of short periods.

[16] Steady state analytical solutions for airglow perturbations by gravity waves have also been used [e.g., *Swenson and Gardner*, 1998; *Liu and Swenson*, 2003; *Vargas et al.*, 2007] to obtain generalized analytical estimates of cancellation factor for gravity wave momentum flux calculations. For these studies, empirical photochemistry models based on in situ rocket measurements were used [*McDade et al.*, 1986, 1987; *Murtagh et al.*, 1990]. Gravity wave forcing was then introduced through the variation of temperature-dependent reaction rates and density perturbations to minor species. Under this approach, it is assumed that the chemical response occurs on time scales much faster than the gravity wave perturbation, and these steady state chemistry models are approximately valid when gravity wave periods are much longer than chemical reaction time scales. For the $O(^1S)$ and O_2 layer emissions, the assumption of steady state chemistry is likely valid at all relevant gravity wave periods [*Makhlouf et al.*, 1998]. In steady state form, the OH emission rate becomes dependent only on perturbations to O, and the effects of H and O_3 are eliminated from the expression for volume emission rate. These assumptions are not valid for short-period waves (τ < 20 min) [e.g., *Liu and Swenson*, 2003]. The lifetime of O_3 participating in the OH excitation reaction is on the order of the Brunt-Väisälä period (~4–6 min) and thus is comparable to the very short wave periods that we wish to study here.

[17] Over the years, a variety of numerical approaches to airglow modeling were developed to obtain emission perturbations from simulated gravity waves. These range from one-dimensional models, considering detailed photochemistry with basic dynamics [e.g., *Hickey and Yu*, 2005, and references therein], to three-dimensional models with basic steady state photochemistry but realistic nonlinear wave dynamics [e.g., *Horinouchi*, 2004]. *Snively and Pasko* [2005] and *Snively et al.* [2007] utilized a model incorporating basic time-dependent chemical kinetics of O_3 to

Table 1. Chemical Reaction and Rates for $O(^1S)$ 557.7 nm Model[a]

Reaction	Rate[b]	Notes
$O + O + M \xrightarrow{k_1} O_2 + M$	$k_1 = 4.7 \times 10^{-33} (300/T)^2$	Three-body production of O_2 (total)
$O + O + M \xrightarrow{\zeta k_1} O_2(c^1\Sigma_u^-) + M$	$\zeta = 0.03$	Three-body production of $O_2(c^1\Sigma_u^-)$
$O_2(c^1\Sigma_u^-) + O_2 \xrightarrow{k_2} O_2(b^1\Sigma_g^+) + O_2$	$k_2 = 5.0 \times 10^{-13}$	Quenching of $O_2(c^1\Sigma_u^-)$ by O_2
$O_2(c^1\Sigma_u^-) + O \xrightarrow{k_3} O_2 + O$	$k_3 = 6.0 \times 10^{-12}$	Quenching of $O_2(c^1\Sigma_u^-)$ by O
$O_2(c^1\Sigma_u^-) + O \xrightarrow{\delta k_3} O_2 + O(^1S)$	$\delta = 0.2$	Fractional excitation of $O(^1S)$
$O_2(c^1\Sigma_u^-) \xrightarrow{A_1} O_2 + h\nu$	$A_1 = 2.0 \times 10^{-2}$	Radiative loss of $O_2(c^1\Sigma_u^-)$
$O(^1S) + O_2 \xrightarrow{k_4} O(^3P) + O_2$	$k_4 = 4.0 \times 10^{-12} \exp(-865/T)$	Quenching of $O(^1S)$
$O(^1S) \xrightarrow{A_2} O + h\nu$	$A_2 = 1.105$ (1.35)	Radiative loss of $O(^1S)$ at all λ
$O(^1S) \xrightarrow{A_{5577}} O + h\nu$ (557.7 nm)	$A_{5577} = 1.06$ (1.18)	Radiative loss of $O(^1S)$ at 557.7 nm

[a]Based on the work of *Bates* [1988] and *Hickey et al.* [1997] and references cited therein.
[b]Einstein coefficients A_2, A_{5577} in parentheses are specified from *Nicolaides et al.* [1971], and used here to allow comparison with results of *Murtagh et al.* [1990], *Makhlouf et al.* [1998], and *Snively et al.* [2007]. Temperature T is given in units Kelvin; units for unimolecular reaction rates are s^{-1}, for two-body reaction rates are $cm^3\ s^{-1}$, and for three-body reaction rates are $cm^6\ s^{-1}$.

obtain simple solutions for the OH(8,3) emission rate. A steady state model was used for the OI 557.7 nm emission, and passive advection of atomic oxygen was considered. These photochemical models were based on the work of *McDade et al.* [1986, 1987], using an approach similar to that of *Horinouchi* [2004]. Gravity wave dynamics were implemented using velocity fields and density perturbations obtained from the fully nonlinear numerical dynamics model, initialized with ambient profiles provided by MSISE90 [*Hedin*, 1991].

2. Model Development

[18] The present study expands existing models [e.g., *Snively and Pasko*, 2005; *Snively et al.*, 2007] to include the full OH(v) band system and realistic $O(^1S)$ photochemistry [e.g., *Makhlouf et al.*, 1995; *Adler-Golden*, 1997; *Makhlouf et al.*, 1998; *Hickey et al.*, 1997] to facilitate fast calculation of OH Meinel bands and OI 557.7 nm airglow emissions for gravity waves simulated within the nonlinear dynamics model. Using these models, detailed descriptions of minor species density and photon emission rate perturbations are obtained for the OH and OI airglow layers, along with column-integrated airglow intensity and brightness-weighted temperature signatures, for ducted waves at different altitudes of trapping and different model configurations.

2.1. Photochemical Models

[19] The number densities n of associated minor species are determined by Eulerian continuity equations of the form

$$\frac{\partial n}{\partial t} = P - L - \nabla \cdot (n\vec{v}), \tag{5}$$

where $\vec{v}$ is the velocity of the background major gas perturbed by gravity waves. At mesopause altitudes, it is assumed that all species have the same kinetic temperature and velocity as the background major gas. The terms P and L are rates of volumetric production and loss of minor constituents by chemical reactions [*Walterscheid et al.*, 1987; *Makhlouf et al.*, 1995], and L is a function of n. In addition to changes in concentrations of reacting species owing to advection by the gravity wave velocity field $\vec{u}$, the effects of gravity waves on airglow emissions are also introduced through the associated temperature-dependent reaction rates.

[20] For the modeling studies here, only species with lifetimes on the order of gravity wave time scales, H and O_3, are treated in a fully time-dependent fashion, including all terms in equation (5). Species with short lifetimes (on the order of seconds or faster) are treated under the assumption that an evolving chemical steady state is maintained during the course of gravity wave perturbations while the advective term is neglected. Major and minor species with lifetimes on the order of hours or days experience advection by the gravity waves, while the losses (and production) by photochemistry (P and L) are assumed negligible. These model assumptions are specified to be consistent with findings by *Makhlouf et al.* [1995, 1998] and *Snively and Pasko* [2005], specifically that dominant OH chemical time dependence is imposed through reactions of H and O_3, and that OI chemistry exhibits time scales much faster than gravity wave processes. These assumptions are discussed in detail in sections 2.1.1 and 2.1.2.

[21] An effect not accounted for is the exothermic chemical heating due to gravity wave-induced perturbations of the airglow layers; it was suggested that waves may be destabilized by photochemical feedback effects, particularly for longer vertical wavelengths [*Xu et al.*, 2001]. These interactions between gravity waves and chemistry may be of interest for future studies. However, these effects may remain relatively weak for the case studies here owing to relatively high mesopause temperature and viscosity [*Xu et al.*, 2001] and limited vertical propagation owing to strong confinement of the waves by the prescribed Doppler ducts.

2.1.1. OI Airglow Model

[22] For our studies of wave-induced modulation of the 557.7 nm $O(^1S)$ emission, a chemical model derived from that used by *Hickey et al.* [1997, and references therein] and *Schubert et al.* [1999, and references therein] is implemented as shown in Table 1. Reaction k_1 describes the three-body production of O_2, where ζk_1 describes the fraction of $O_2(c^1\Sigma_u^-)$ produced that serves as a precursor for production of $O(^1S)$. Reactions k_2, k_3, and A_1 describe sinks for the precursor $O_2(c^1\Sigma_u^-)$, where δk_3 represents the fraction of $O_2(c^1\Sigma_u^-)$ quenching by O leading to $O(^1S)$ production. Reaction k_4 describes quenching of $O(^1S)$ by O_2. Reaction A_2 describes the total radiative loss of $O(^1S)$ at both 557.7 nm and 297.2 nm wavelengths, where A_{5577} denotes radiative loss contributing to the 557.7 nm green line emission.

[23] In contrast to the case of OH photochemistry discussed in section 2.2.2, the $O(^1S)$ excitation and emission processes occur over time scales much shorter than a gravity wave period, on the order of seconds or faster [e.g., *Makhlouf*

Table 2. Chemical Reactions and Rates for OH(v) Model[a]

Reaction	Rate[b]	Notes
$H + O_3 \xrightarrow{k_{5v}} OH(v) + O_2$	$k_{5v} = 1.4 \times 10^{-10} \exp(-470/T)\ b(v)$	Branching ratios b (v) given by *Makhlouf et al.* [1995, Table 1]
$O + O_2 + M \xrightarrow{k_6} O_3 + M$	$k_6 = 6.0 \times 10^{-34}\ (300/T)^{2.3}$	Three-body production of O_3 [*Makhlouf et al.*, 1995]
$OH(v') + O \xrightarrow{k_{7v'}} H + O_2$	$k_{7v'} = a_7\ (v') \times 10^{-11}$	Quenching rates $a_7 v'$ given by *Makhlouf et al.* [1995, Table 1]
$OH(v') + O_2 \xrightarrow{k_{8v',v''}} OH(v'') + O_2$	$k_{8v',v''} = a_8\ (v', v'') \times 10^{-13}$	Quenching rates $a_8(v', v'')$ given by *Adler-Golden* [1997, Table 3]
$OH(v') + N_2 \xrightarrow{k_{9v'}} OH(v'') + N_2$	$k_{9v'} = a_9\ (v') \times 10^{-14}$	Quenching rates $a_9(v')$ given by *Adler-Golden* [1997, Table 1]
$OH(v') \xrightarrow{A_{v',v''}} OH(v'') + h\nu$	$A_{v',v''}$	Band-averaged Einstein coefficients for transition v' to $v'' = v' - n$ given by *Turnbull and Lowe* [1989, Table 1] with correction of *Adler-Golden* [1997].

[a]Based on the work of *Makhlouf et al.* [1995] and *Adler-Golden* [1997] and references cited therein.
[b]Temperature T given in units Kelvin; units for unimolecular reaction rates are s^{-1}, for two-body reaction rates are $cm^3\ s^{-1}$, and for three-body reaction rates are $cm^6\ s^{-1}$.

et al., 1998]. O(^1S) and its precursor thus have lifetimes that are very short compared to relevant gravity wave processes, and O has a lifetime longer than a typical model simulation run (and nighttime observation period). Time-dependent dynamics for the OI model are incorporated through numerically modeled perturbations to minor and major species densities via advection (O, N_2, and O_2) and to model kinetic temperatures affecting reaction rates. Resulting photon emission rate perturbations are then obtained under the assumption that a chemical steady state is maintained, which evolves with the gravity wave dynamics. These assumptions are consistent with findings of *Makhlouf et al.* [1998] that chemical time dependence does not play a meaningful role in determining the OI airglow signature.

2.1.2. Multiband OH(v) Model

[24] The basic OH model used in this paper is derived from the works of *Makhlouf et al.* [1995] and *Adler-Golden* [1997] and consists of the system of chemical equations listed in Table 2. Reaction k_5 is generally believed to be the primary reaction producing OH($v \geq 6$) [*Adler-Golden*, 1997, and references therein] and is the dominant sink for O_3 at mesopause altitudes [e.g., *Smith et al.*, 2008]. Production of O_3 occurs via reaction k_6, leading to an approximately balanced state with k_5 at long time scales (~1 h) [*Liu and Swenson*, 2003]. The loss of OH(v) molecules occurs through chemical quenching by O (reaction $k_{7v'}$), and quenching by O_2 and N_2 (reactions $k_{8v',v''}$ and $k_{9v'}$, respectively), and radiative loss (reaction A(v′, v″)). The set of reactions k_5–$k_{9v'}$ represents dominant reactions governing minor species OH, H, O_3, O, and vibrationally excited OH(v) [e.g., *Makhlouf et al.*, 1995]. Excitation of OH via HO_2 discussed briefly in section 1.2 is not included in the airglow model, because the lower vibrational states are populated through quenching of higher vibrational states [*Adler-Golden*, 1997] and these lowest vibrational states do not contribute to the emissions most commonly observed by visible-range ground-based imagers. For studies of infrared OH band emissions, for example arising from vibrational states $v \leq 3$, reactions associated with HO_2 should be considered. Infrared OH signatures of gravity waves are investigated in a separate paper.

[25] The OH photochemical model developed here makes several simplifying assumptions to permit rapid calculation of emissions rates within the numerical dynamics model. Chemical lifetimes of H and O_3 within the emitting region are on the order of ~4–6 min, consistent with the gravity wave Brunt-Väisälä period. For the short-period ducted waves considered here, it is essential to account for time dependence via chemical production and losses, and also advection, by solving the full continuity equation (5) for H and O_3. As noted by *Makhlouf et al.* [1995], advection does not significantly influence the short-lived excited OH(v = 0–9) within the airglow layer, which achieves chemical steady state conditions that evolve with the gravity wave perturbations. For long-lived major species [M = (N_2, O_2), O], P and L may be set to zero, while the advection term is taken into consideration. These simplifications dramatically reduce computational expense by allowing the use of a less costly "explicit" rather than "implicit" numerical solution that does not require iteration to obtain cell update values between time steps.

2.2. Gravity Wave Dynamics Model

[26] Numerical simulation results are obtained with the model presented by *Snively and Pasko* [2003, 2008] describing the compressible, nonlinear, and stratified Euler equations in conservation law form. They are calculated using a modified version of the freely available CLAWPACK software package (available at http://www.amath.washington.edu/claw) [*LeVeque*, 2002]. Using an explicit time-split method, viscosity and thermal conduction terms are introduced, along with gravity wave forcing terms and chemical production and loss. For boundary conditions, the model is run with "open" top and side boundaries, with a reflective ground surface, and without the use of sponge layers. The domain extends from 0 to +600 km in the horizontal direction, and 0 to 220 km in the vertical direction, with 0.5 km uniform resolution (Δx and Δz).

[27] Increasing molecular kinematic viscosity at high altitude naturally damps waves that propagate vertically toward the upper boundary, reducing artificial reflection. At lower altitudes (below ~110 km), the kinematic viscosity is fixed at a value that is comparable to or slightly greater than measured eddy diffusion throughout the middle atmosphere ($100\ m^2\ s^{-1}$) [e.g., *Hocking*, 1990; *Fukao et al.*, 1994]. At altitudes above those where eddy diffusion dominates, the total diffusion coefficient is dominated by the molecular kinematic viscosity, which is estimated by assuming that it is inversely proportional to the decreasing atmospheric density [*Gossard and Hooke*, 1975, p. 222]. Figure 5 in the work of *Snively and Pasko* [2008] depicts the model viscosity profile. At mesopause altitudes, however, total viscous dissipation remains relatively weak and does not strongly influence the solution. To prevent evolution of the ambient atmosphere, the solutions for viscosity and thermal conduction are applied only to perturbations of the initial state.

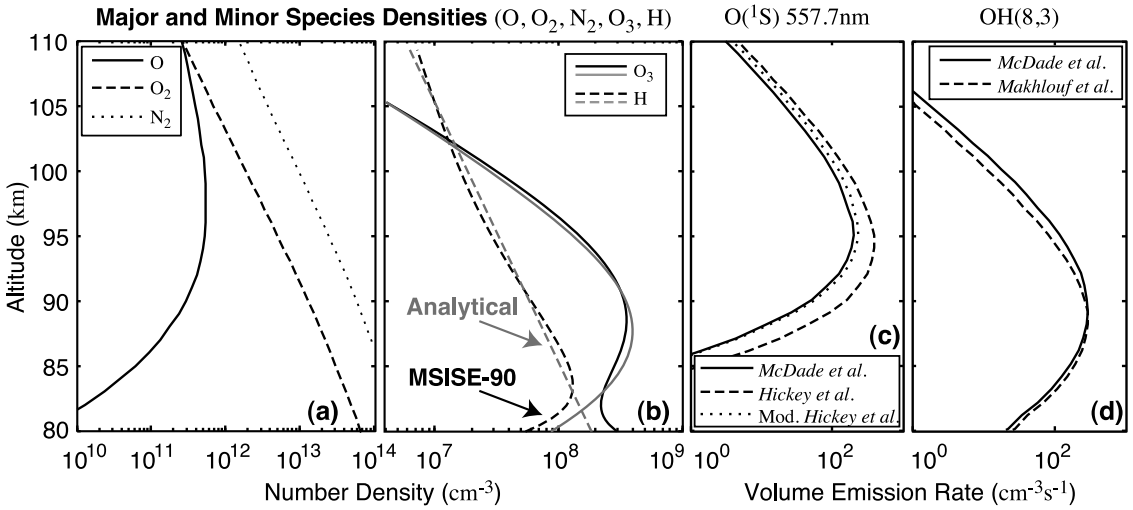

Figure 2. (a) Major and (b) minor species densities used in the OH and OI models, as obtained from MSISE-90 [*Hedin*, 1991]. Photon volume emission rates are depicted for (c) O(^1S) and (d) OH(8,3) emissions, derived from the specified species profiles.

[28] The dynamical model also calculates density perturbations of minor species, which participate in the photochemistry. Using a nonlinear advection solver [*LeVeque*, 2002] coupled to the main gravity wave dynamics code, H, O_3, and O are perturbed with the fluid motions under the assumption that all species share the same velocities. As discussed previously in section 2.1, the densities of species H and O_3 are simultaneously dependent on chemical production and loss processes via the continuity equation (5). The photochemical model component carries ~50% computational penalty beyond using the dynamics model alone.

2.3. Ambient Atmosphere

[29] Background atmospheric conditions use MSISE90 temperature and neutral density fields [*Hedin*, 1991], obtained for 5 July 2003, specified at the Maui-MALT observatory at the summit of Haleakala Crater, Maui, Hawaii (20.7°N, 156.3°W). These conditions agree with a typical night of observation on which short-period gravity wave signatures were detected [*Simkhada et al.*, 2009].

[30] Figures 2a and 2b depict the major and minor species densities associated with the MSIS profile. When obtaining an O_3 initial steady state profile directly from available MSIS data, O_3 density approaches infinity where H density approaches zero in the mesosphere. Under these conditions, a shallow density minimum of O_3 arises at 83 km, compared to a typically deeper minimum occurring between 75 and 80 km altitude seen in observational data [e.g., *Smith et al.*, 2008]. To allow the O_3 profile to maintain a realistic profile shape above 80 km (where the OH photochemistry is active), a profile of H that decays exponentially in the vertical is first fit to the MSIS layer-shaped profile. From this fit profile, a new O_3 profile is determined under steady state assumptions, which approaches zero rather than infinity at low altitudes. For the main calculations reported here, the MSIS H profile is used in model calculations. The profiles are then held in balance by subtracting any initial tendency that would lead to evolution to a new steady state [*Huang and Hickey*, 2007]. This correction remains small at peak OH altitudes and increases at lower altitudes. This method allows both H and O_3 to exhibit physical layer-like structure above 80 km, without producing discontinuities at lower altitudes and without the need for a full description of chemistry below the OH layer region. Tests (not shown) reveal that use of the exponentially decreasing profile of H result in a less physical altitude profile of volume emission rate, where the MSIS H profile yields volume emission rates more closely in agreement with past observational and modeling studies [e.g., *McDade et al.*, 1987; *Makhlouf et al.*, 1995; *Adler-Golden*, 1997].

[31] Figure 2c depicts the initial steady state emission profiles of the OI emission, comparing models of *McDade et al.* [1986] with that of *Hickey et al.* [1997]. To allow direct comparisons with present results and those from *Snively et al.* [2007], different Einstein coefficients A_2 and A_{5577} are specified in the "modified" chemical scheme. These values are those in parentheses in Table 1, attributed to *Nicolaides et al.* [1971]. Figure 2d depicts a comparison of *McDade et al.* [1987] and *Adler-Golden* [1997] chemistries for calculation of the OH(8,3) emission, showing good agreement except for slightly different peak altitudes. The modeling approach based on the work of *Makhlouf et al.* [1995] and *Adler-Golden* [1997] leads to more complete description of the OH(v) kinetics, permitting calculation of multiple OH band emission rates.

[32] Figures 3a and 3b depict OH(v) vibrational states 1–9, revealing significant variation in altitudes and number densities for different states. Greater concentrations of higher states exist at higher altitudes, leading to different peak emission altitudes for specific bands [i.e., OH(8,3), OH(6,2), and OH(3,1)] commonly observed by ground-based instruments. Although airglow imaging studies often compare gravity wave signatures arising from single OH bands (or groups of bands) with adjacent OI and O_2 layer emissions, comparison of separate OH bands arising from different vibrational transitions may also provide important insight into wave structure over altitude.

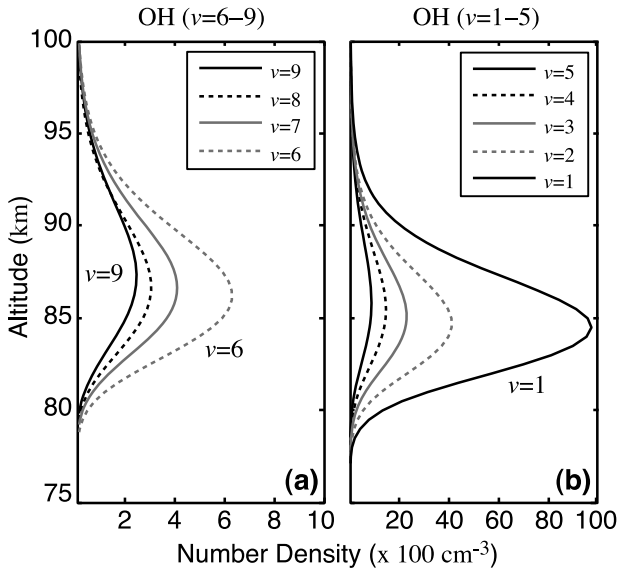

Figure 3. OH(v) vibrational level densities.

2.4. Source Characteristics and Model Parameters

[33] Waves are generated using a vertical forcing applied by an idealized momentum source located within the duct. The source applies a traveling wave forcing in the horizontal direction, with vertically standing (zero-node) structure, constrained by a Gaussian envelope. Waves are excited principally in the "rightward" horizontal direction (i.e., toward the right of the simulation domain). The source of the gravity waves is positioned at x_o = 200 km and z_o = 80, 90, or 100 km, with peak forcing occurring at t_o = 25 min. It provides a vertical force at a chosen frequency (ω) and horizontal wave number (k_x) of the form $\sim\exp[-(x - x_o)^2/2\sigma_x^2 - (z - z_o)^2/2\sigma_z^2 - (t - t_o)^2/2\sigma_t^2]\cos[\omega t - k_x(x - x_o)]$, where σ_x and σ_z are the Gaussian envelope's horizontal and vertical half widths, respectively, and σ_t is the temporal Gaussian half width; the position given by x_o, z_o, and t_o corresponds to the source maximum in space and time.

[34] The source characteristics are consistent with observed ground-relative wave parameters of ducted gravity waves near the Brunt-Väisälä frequency. For the ducted wave case study, the following parameters are defined: ω = 0.0238 rad/s (ground-relative T = 4.4 min), $k_x = 3.14 \times 10^{-4}$ rad/m (λ_x = 20 km), σ_x = 30 km, σ_z = 3 km, and σ_t = 5 min. The sources are tuned to produce waves of approximately 5 K peak temperature perturbations.

[35] Figure 4a depicts ambient wind profiles specified for each duct, each of identical shape but different peak altitudes (80, 90, and 100 km). Functions are defined by identical sinusoids enveloped by Gaussian functions, each centered at 80, 90, or 100 km. A constant background wind offset is specified throughout the domain to enhance trapping of the waves. Figure 4b depicts the ambient temperature, showing mesopause at approximately 87 km altitude, along with Brunt-Väisälä period plotted over the same range. The lower-thermospheric thermal duct is apparent at approximately 115 km altitude [e.g., *Walterscheid et al.*, 2001]. Figure 4c illustrates the three duct characteristics given by the vertical wave number m^2 of the Taylor-Goldstein equation for τ = 4.4 min and λ_x = 20 km, where regions of $m^2 < 0$ denote evanescent boundaries.

[36] Slight differences between ducts arise owing to varying thermal conditions; however, the ducting is due almost entirely to the strong wind field and the very short wave period. As a result, the characteristics of each duct (at 80, 90, and 100 km altitudes) are similar; all simulations depict waves that are nonideally ducted waves close in characteristics to fundamental mode solutions (i.e., no nodes in the vertical velocity field). If not stated otherwise, results depicted are plotted at a time 50 min after the start of the simulation run, after the wave has propagated a distance of approximately three horizontal wavelengths.

3. Results and Discussion

[37] The discussion focuses on comparison of airglow perturbations and resulting signatures for trapped waves at 80, 90, and 100 km altitudes. Additional control cases are performed in which effects are selectively turned off for comparison, each for a wave at 90 km altitude. These include 90NC (chemical time dependence disabled, dynamics only), 90H (hydrogen layer replaced with constant exponential

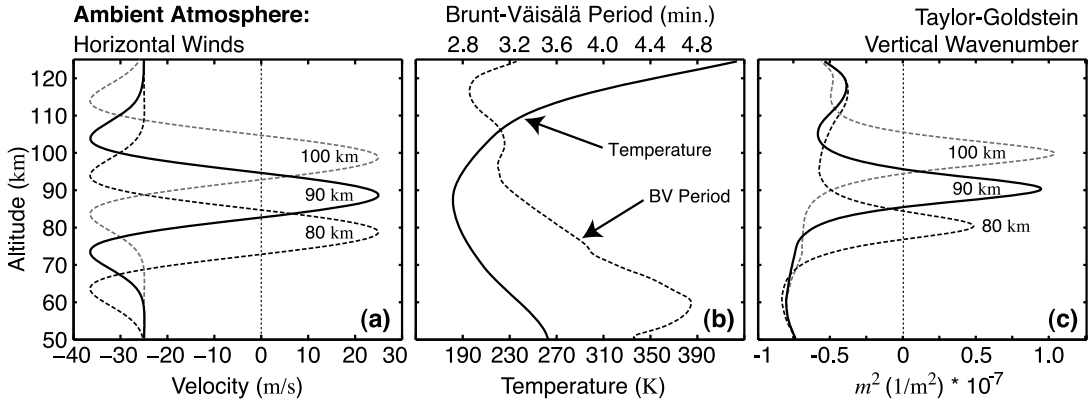

Figure 4. (a) Analytically specified Doppler duct wind profiles for 100, 90, and 80 km ducts; (b) ambient MSISE-90 temperature (solid curve) and Brunt-Väisälä period (dashed curve) profiles; and (c) corresponding profiles of m^2.

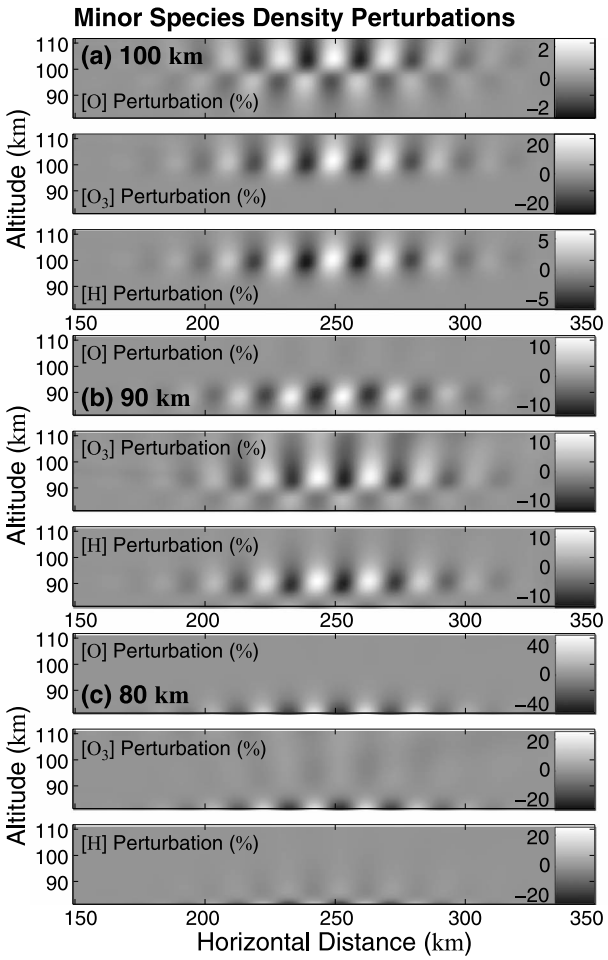

Figure 5. Density perturbations of O, O_3, and H for ducted waves at three altitudes: (a) 100, (b) 90, and (c) 80 km.

decay), and 90LIN (wave magnitude reduced by a factor of 10).

[38] The case studies were designed to investigate wave perturbations arising from different altitudes, for waves that do not contain phase reversals of vertical velocity fields with altitude. The simple packets induce only alternating up and down perturbations to the flow, and they illustrate a near-ideal case of ducting near a fundamental mode. First, we consider three cases, for ducts with centers specified at 80, 90, and 100 km, respectively. Second, we investigate the nonlinearity of the OH layer response for strong wave perturbations, which is enhanced by steep gradients of O_3 and H.

3.1. OH and OI Dependence on Ducting Altitude

[39] It is important to distinguish between wave perturbations that lead to vertical displacements of layers and those that distort the shapes of only upper or lower halves of layers. Owing to the finite thickness of emission regions, ducted waves that are vertically confined may not extend fully within the layer vertical expanses, perturbing only the tops or bottoms. These perturbations are determined partially by the local gradients of minor species, in addition to the phase of the wave-induced perturbations. A large percent change of species density may arise from a localized perturbation at a steep gradient. Whether this leads to a strong integrated intensity response is determined by the resulting percent change of the volume emission rate relative to the total. Localized perturbations to only half of a layer are less likely to experience vertical cancellation effects, such that a wave packet concentrated near the OI layer region may still produce a measurable (albeit weak) perturbation to the hydroxyl layer and vice versa. These effects are clearly exhibited in all cases simulated here.

3.1.1. Density Perturbations

[40] We first examine density perturbations to three minor species layers that play dominant roles in airglow perturbations. OH layer variations due to small-scale waves are controlled by H and O_3 density and perturbations and, at longer periods, perturbations to O are likely to dominate [e.g., *Liu and Swenson*, 2003]. The OI emissions are significantly influenced by perturbations to O number density.

[41] Figure 5a depicts three panels showing wave-induced percent density perturbations of O, O_3, and H density for the wave centered at 100 km altitude. The resulting perturbation of the O density is consistent with alternating upward and downward displacements of the layer. The alternating perturbations are centered about the peak of the layer near 100 km altitude. Only the tops of the O_3 and H layers are perturbed by the same wave, such that their density perturbations do not clearly exhibit the distinctly opposite relative perturbations across the density peak. The very strong percent change in O_3 density is a consequence of the relatively low density above the layer peak and of the steep gradient.

[42] Figure 5b depicts density perturbations for the wave centered at 90 km. Here, the dominant perturbation to the O layer occurs at the bottom of the layer, with relatively weak changes in density above the layer peak. As was the case with O_3 and H at 100 km, the layer has been distorted rather than fully lifted or depressed. Here, the O_3 perturbation exhibits strong structure across the layer peak, which occurs near the wave packet center. Similar structure is visible, albeit weaker, for the H layer, and dominant perturbations involve distortions to the upper portion of the layer.

[43] Figure 5c depicts density perturbations for the wave centered at 80 km. Strong relative perturbations of O exist at low altitudes, and the dominant relative perturbation occurs well below the 100 km layer peak. However, it is notable that large percent density perturbations here are consistent with relatively weak species perturbations due to lower ambient density of O at these low altitudes. Both O_3 and H exhibit structure above and below the layer peak, although the wave packet is concentrated principally below. For these cases, the density percent perturbations are enhanced by the low ambient densities on the bottom sides of the layers, and steep gradients. This leads to large variations that do not necessarily indicate large resulting intensity perturbations (particularly in the case of the OI emission).

3.1.2. Emission Rate Perturbations

[44] Resulting emission rate perturbations are obtained from postprocessing of temperature and density fields calculated by the dynamics model. Steady state one-dimensional volume emission rate profiles are first obtained, such as those depicted in Figures 2c and 2d, to allow calculation of relative perturbations. Next, the perturbed two-dimensional

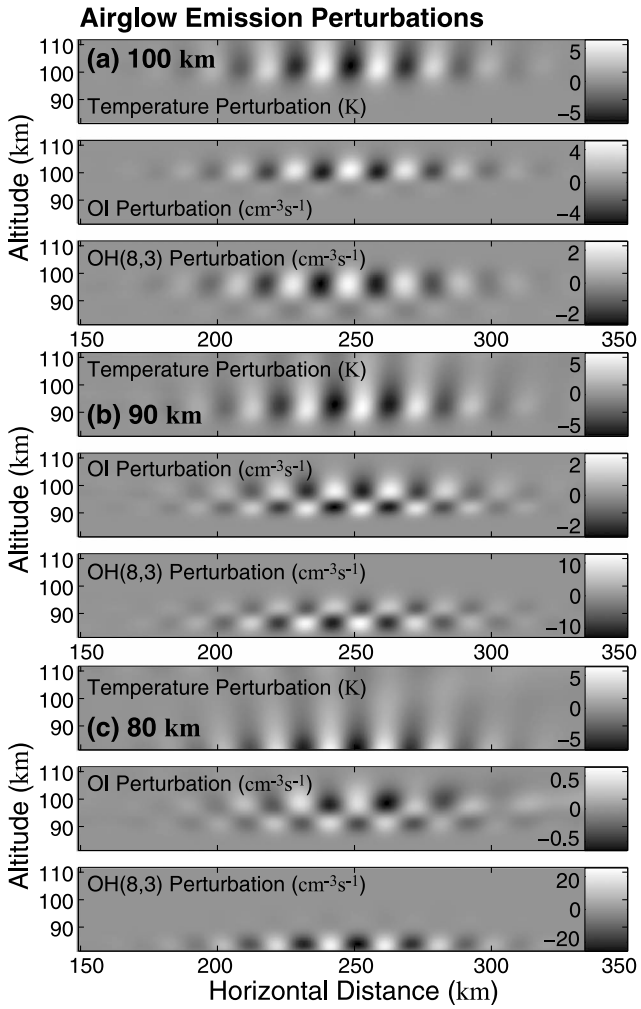

Figure 6. Temperature, OI, and OH(8,3) photon emission rate perturbations for ducted waves at three altitudes: (a) 100, (b) 90, and (c) 80 km.

volume emission rates are obtained at a time 50 min into the simulation (25 min following the excitation of the wave packets). The emission rate perturbations arise from wave perturbations to density and temperature, and are determined by both the minor species (O, O_3, and H) and mean major species (O_2, N_2) density fluctuations, which influence reaction rates and modulate relative densities. While OH(8,3) emission rates are calculated here, emissions resulting from other vibrational bands may be obtained easily.

[45] Figure 6a depicts three panels showing wave-induced perturbations of kinetic temperature, OI volume emission rate, and OH(8,3) volume emission rate. The local temperature perturbation indicates that the wave structure concentrated near 100 km altitude, and therefore well above the ~87 km mesopause temperature minimum. Dominant OI perturbations and OH(8,3) perturbations occur at the tops of the layers. Although the OI perturbation is centered around the layer peak, the wave temperature perturbations extend higher and lead to dominance of signatures from the top of the layer. This case, where the wave packet is trapped principally above the airglow layers, is likely very common given the strong lower-thermospheric duct present just above mesopause under typical conditions [e.g., *Walterscheid et al.*, 2001].

[46] Figure 6b depicts perturbations for the wave centered at 90 km, revealing OI and OH(8,3) signatures consistent with full-layer perturbations. Both layers exhibit alternating enhancements and depletions, complementary about the layer centers. Variations in total integrated photon emission rate will be highly sensitive to the exact position of the wave relative to the minor species participating in photochemistry.

[47] Figure 6c depicts perturbations for the wave centered at 80 km. Despite the low altitude of the wave, weak layer perturbations to the OI emission are visible due to the evanescent signatures above the duct. A strong OH(8,3) signature arises at ~85 km near and below the peak of the emission. As dominant perturbations here occur without significant cancellation from higher altitudes, this can be expected to lead to strong measurable wave-induced intensity perturbations in the integrated signature.

3.1.3. Integrated Signatures

[48] Photon volume emission rate $\varepsilon(x, y, z, t)$ (cm^{-3} s^{-1}) can be vertically integrated to determine the total column emission rate $I(x, y, t)$ (cm^{-2} s^{-1}) for zenith observations, as would be observed by ground-based imagers and photometers. Although the model is two-dimensional, the numerical solutions may be thought of as infinitely extended in the third (y) direction, with each cell representing a volume cube. Neglecting line-of-sight effects of off-axis viewing, and curvature of the Earth, we can define I simply as

$$I(x,t) = \int_{z_1}^{z_2} \varepsilon(x,z,t)dz. \tag{6}$$

An additional parameter of interest is brightness-weighted temperature $T_I(x, t)$, which is analogous to the temperature inferred via measurement of adjacent rotational lines in the OH vibrational band spectrum [e.g., *Meriwether*, 1984; *Makhlouf et al.*, 1995]. These quantities differ slightly in practice; however, T_I serves as a useful proxy for rotational temperature and is defined as

$$T_I(x,t) = \frac{1}{I(x,t)} \int_{z_1}^{z_2} \varepsilon(x,z,t)T(x,z,t)dz. \tag{7}$$

The Krassovsky ratio, which is a complex quantity relating the intensity perturbation to the brightness-weighted temperature perturbation, is defined as

$$|\eta| = \frac{\delta I/\bar{I}}{\delta T_I/\overline{T_I}}, \tag{8}$$

where $\eta = |\eta|\exp[j(\phi_I - \phi_T)]$ and $\phi = \phi_I - \phi_T$ denotes the phase shift between intensity and brightness-weighted temperature. Typically, ϕ is equal to approximately 0° or 180° (in-phase or antiphase) for ideally ducted waves due to vertical cancellation of phase shift in the integrated signatures [*Hines and Tarasick*, 1994; *Snively and Pasko*, 2005]. Here, we calculate integrated intensity I and brightness-weighted temperature T_I for the case studies of waves at 80, 90, and 100 km, respectively, and investigate the variations in Krassovsky ratio amplitude and phase for OH and OI emissions.

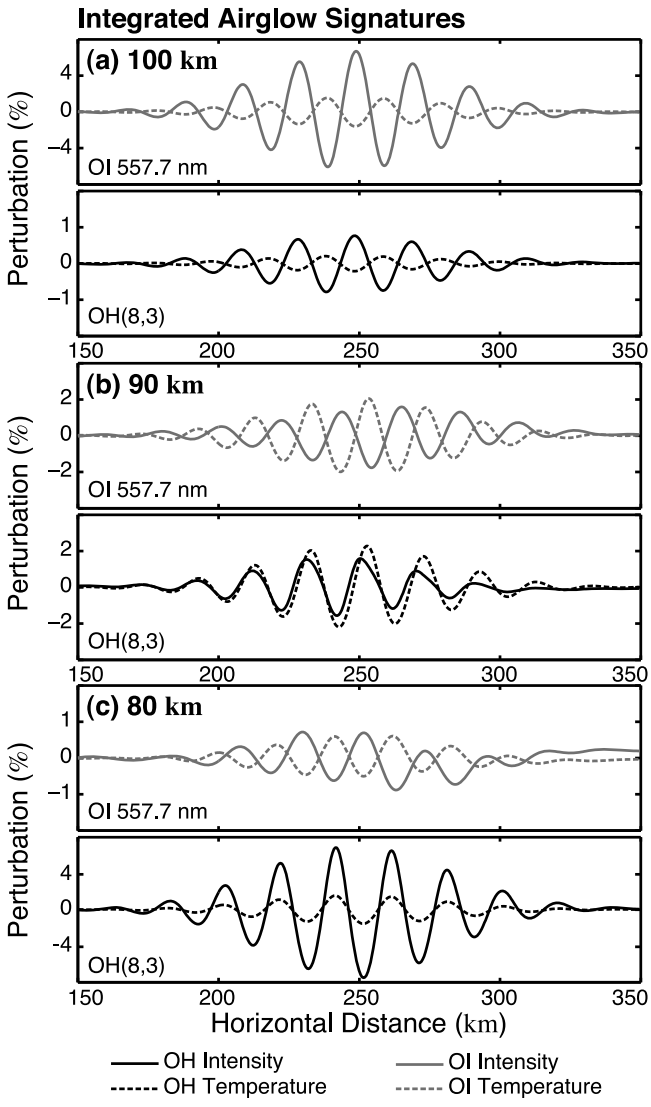

Figure 7. Integrated OI 557.7 nm and OH(8,3) photon emission rate and brightness-weighted temperature perturbations for ducted waves at three altitudes: (a) 100, (b) 90, and (c) 80 km.

[49] Figure 7a depicts the total integrated response for waves at 100 km altitude. An important feature of the data is that both emissions exhibit antiphase Krassovsky ratios and are in phase with each other. In both cases, T_I perturbations are weaker than the relative I perturbations. The OI emission perturbations, due to high altitude of the duct and reduced cancellation, are notably stronger in amplitude. The large magnitude of the Krassovsky ratios is consistent with the relatively limited cancellation effects for both signatures.

[50] Figure 7b depicts the integrated response for waves at 90 km altitude. Here, both OH and OI emissions intensities exhibit similar amplitude response in I and T_I. However, the antiphase Krassovsky ratio for the OI emission leads to reversal of phase when comparing OH and OI layer responses. Intensity and brightness-weighted temperature perturbation amplitudes for each emission are approximately equal, such that $\eta \simeq 1$.

[51] Figure 7c depicts the integrated response for waves at 80 km altitude, finding the antiphase Krassovsky ratio for the OI emission. The OH emission perturbations, because of the low altitude of the duct and reduced cancellation, are notably stronger in amplitude and equivalent to the strong OI perturbations seen in the 100 km case.

[52] This phase reversal is consistent with effects predicted by *Hines and Tarasick* [1994] and demonstrated by *Snively and Pasko* [2005] and is here seen for waves with dominant perturbations near 90 km altitude or below. The case of *Snively and Pasko* [2005], however, is limited by an overly simplistic description of minor species dynamics; the chemical model, based on the work of *McDade et al.* [1986, 1987], does lead to similar results to the model used here when dynamics are treated equally. Validation tests were performed (although not shown here) using the simplified chemistry models of *Snively and Pasko* [2005] and *Snively et al.* [2007] and were found to lead to nearly identical responses with slightly different peak altitudes of emission.

[53] Both amplitude and phase, for OH and OI emissions, will vary depending on the local profiles of minor species participating in the photochemistry, and the altitude of wave perturbations relative to the chemistry. The OI emission will be dependent on the ambient state and wave-induced perturbations of O; likewise, the OH emission will depend on H and O_3. This suggests both seasonal and regional variability in the responses, dependent on both the chemical density profiles over altitude and the background temperature and wind structure that lead to wave trapping. These effects are especially prominent for the case of short-period wave perturbations. For the ducted waves shown, the wave perturbation of vertical velocity is strong, such that upward and downward displacements of the layers play a significant role in the emission intensity perturbations. The effects of the vertical perturbations are strongly dependent on the layer shapes and gradients.

[54] Some generalizations about the airglow responses may be made. First, for waves such as those simulated (showing approximate zero-node standing wave structure), the OI layer tends to exhibit an antiphase Krassovsky ratio, consistent with results of *Snively and Pasko* [2005]. Second, the OH layer tends to exhibit an in-phase Krassovsky ratio when the dominant wave perturbation arises within or below the layer, and an antiphase ratio when arising principally from the top. Therefore, waves trapped at higher altitude, for example in the lower-thermospheric duct, may be less likely to produce antiphase OH and OI signatures than those trapped in inversion layers near ~80–90 km. As originally suggested by *Snively and Pasko* [2005], results imply that waves categorized as "mesospheric bores" need not exhibit distinct phase reversals of wave vertical velocity between the airglow layers to produce an antiphase airglow signature. The antiphase OH and OI signatures do not necessarily indicate antiphase wave perturbations, but they are a consequence of the interplay of airglow chemistry and wave-induced perturbations against minor species density gradients.

[55] Simultaneous measurements of brightness-weighted temperature, detailed characterizations of ambient temperature and wind fields, and multistation measurements facilitating triangulation or tomography may provide important insight into actual standing wave structure and associated

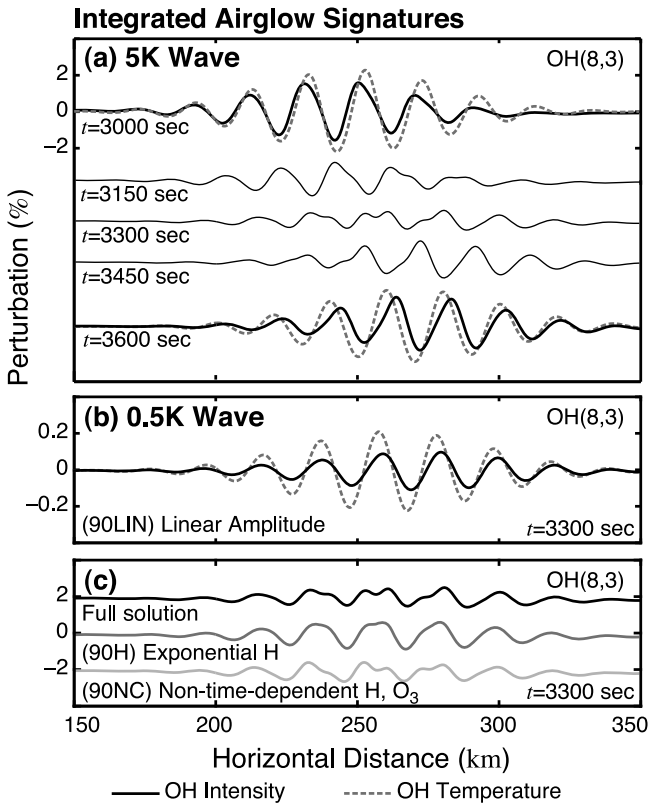

Figure 8. Integrated OH(8,3) photon emission rate and brightness-weighted temperature perturbations for ducted waves at 90 km altitude, for (a) 5 K wave temperature perturbation, (b) 0.5 K wave temperature perturbation (90LIN), and (c) test cases comparing the full solution, exponentially decreasing H density profile (90H), and the simplified H and O_3 models which neglect the time dependence of chemical production and loss (90NC).

airglow signatures. For example, both magnitude and phase of the Krassovsky ratio can help to identify the altitude of trapping in the OH layer. For cases where lidar wind and temperature data are available, along with two-dimensional OH rotational temperature and intensity measurements, it may be possible to simulate gravity wave events at a very high level of accuracy, including determination of wave amplitude and vertical structure.

3.2. OH Nonlinear Response

[56] An important feature of the OH response for the 90 km case is a visible distortion of the I signature, shown in Figures 7b and 8, which is otherwise sinusoidal. This is not apparent in the T_I signature. Asymmetry of the response suggests the presence of even-order superposed harmonics (i.e., principally at twice the period and wave number of the perturbing wave). Second-order nonlinearity has been demonstrated for the OH airglow response by *Huang et al.* [2003] as a result of the very steep gradients above and below O_3 and H density maxima near mesopause. This leads to harmonics in the wave-induced density perturbations of the minor species, which are not present in the major gas density perturbations by the wave.

[57] Figure 8a depicts the integrated OH wave signature at five time steps, taken at half-period intervals. The initial T_I signature appears linear throughout the evolution; hence, it is shown only for the first and last steps shown. The amplitude of the intensity is modulated by both the superposed harmonic components and the vertical cancellation within the duct, as perturbations above or below the OH layer occur in opposite phase. The superposed nonlinearity in the intensity signature is especially prominent as the wave vertical cancellation reduces the intensity signature amplitude at t = 3300 s (55 min). This leads to the appearance of smaller-scale structure that is not present in the wave itself, which may falsely suggest that the wave packet is experiencing breaking or resonant interaction [e.g., *Snively and Pasko*, 2008, and references therein].

[58] Several control cases are performed. Figure 8b depicts an equivalent wave perturbation with amplitude reduced by a factor of 10 (case study 90LIN), which does not exhibit such dramatic nonlinearity. It does however still exhibit somewhat diminished intensity relative to the brightness-weighted temperature due to linear cancellation effects. Figure 8c depicts comparisons of the 90 km wave including the full solution for H and O_3 chemistry (90), a solution with the H layer removed using the fit exponentially decreasing profile of Figure 2b (90H), and a solution with realistic profiles but limited description of H and O_3 chemistry (90NC). In the 90NC case, time-dependent kinetics due to P and L terms of equation (5) are omitted. There is a slight phase shift visible in the 90NC solution compared with the full solution; however, the nonlinear components are of comparable magnitude. The 90H solution, however, produces visibly weaker nonlinearity owing to elimination of one steep gradient below the H layer. These effects are consistent with the predictions of *Huang et al.* [2003] and may be observable for waves near the Brunt-Väisälä frequency that are situated within the OH layer region.

[59] The appearance of nonlinearity, principally in the integrated intensity field, suggests that the superposed second-order signature may itself experience varying degrees of cancellation depending on the structure of the wave packet. The T_I brightness-weighted temperature may, or may not, illustrate this nonlinearity depending on the intensity relative to the position of the wave packet. It should be possible to construct multinode wave solutions where cancellation of second-order effects reduces nonlinearity in the intensity signature while producing visible nonlinearity of the brightness-weighted temperature signature. This is facilitated by opposing nonlinear responses from the layer tops and bottoms [*Huang et al.*, 2003], which when integrated may add or subtract depending on the phase of the wave perturbation. These effects may be of observational interest, providing additional means to confirm agreement between modeled and observed airglow signatures, beyond simple comparisons of I and T_I. Further discussion of these observable nonlinear signatures is presented in a separate paper and includes a comparison of modeled and observed data.

4. Conclusions

[60] A two-dimensional and nonlinear photochemical-dynamical model was developed to simulate OH vibrational

and O(^1S) airglow emission perturbations by gravity waves in the mesosphere and lower thermosphere. The model allows he numerical simulation of gravity wave propagation in realistic wind and temperature fields, and calculation of model airglow signatures as would be observed by ground-based imagers.

[61] It is found that airglow perturbations by short-period, small-scale, ducted gravity waves near the Brunt-Väisälä period are primarily determined by density perturbations of minor species. Perturbations of O, O_3, and H contribute significantly to the observed intensity signatures. Where the wave does not fully displace the layers, density perturbations may distort the upper or lower gradients, leading to uncanceled fluctuations in volume emission rate and allowing measurable signatures to arise even where the wave is ~15 km from the layer center.

[62] For ducted waves, the phase of η is found to be a function of both the phase of the wave dynamic perturbations and the position of the packet relative to the gradients of minor species participating in the photochemistry. Comparing the phase of intensity signatures for OI and OH emissions may reveal in-phase or antiphase relationships, depending on the altitude of the packet, and wave characteristics. This suggests that airglow phase relationships are not direct indicators of standing wave mode structure. Events may be more accurately reconstructed with the help of airglow brightness-weighted temperature, or multistation image data, and with available wind and ambient temperature data to define ducting environments. These provide additional constraint on wave amplitudes and propagation environments, allowing close validation of model simulation runs. Ambiguity may still remain owing to variability in minor species profiles, and simulations such as these can benefit from improved descriptions of ambient conditions. These effects likely play a significant role in determining the phase variations of layer intensities observed during mesospheric bore events [e.g., *Taylor et al.*, 1995; *Smith et al.*, 2003].

[63] Strong perturbations may lead to nonlinearity of the airglow signature, even when the dominant wave perturbations are linear with respect to the major gas. This is consistent with theoretical predictions of *Huang et al.* [2003], and the present simulation results suggest that these effects will be observable. These nonlinear effects can provide additional insight into wave characteristics and amplitude, and minor species density profiles. They may also produce signatures that falsely appear to indicate wave breaking or nonlinear interaction effects, leading to potentially erroneous interpretations of observed data.

[64] **Acknowledgments.** This research was supported by NSF grant ATM-04-37140 to the Pennsylvania State University and NSF CEDAR postdoctoral grant ATM-0725317 to Utah State University.

[65] Robert Lysak thanks the reviewers for their assistance in evaluating this manuscript.

References

Adler-Golden, S. (1997), Kinetic parameters for OH nightglow modeling consistent with recent laboratory measurements, *J. Geophys. Res.*, *102*(A9), 19,969–19,976, doi:10.1029/97JA01622.

Barth, C. A. (1961), The 5577 Å airglow emission mechanism, *J. Geophys. Res.*, *66*(3), 985–986.

Barth, C. A. (1964), Three-body reactions, *Ann. Geophys.*, *20*, 181.

Bates, D. R. (1988), Excitation of 557.7 nm OI line in nightglow, *Planet. Space Sci.*, *36*(9), 883–889, doi:10.1016/0032-0633(88)90093-1.

Chamberlain, J. W. (1961), *Physics of the Aurora and Airglow*, AGU, Washington, D. C.

Chimonas, G. H., H. M. Hauser, and R. D. Bennett (1996), The excitation of ducted modes by passing internal waves, *Phys. Fluids*, *8*(6), 1486–1505.

Chung, J. K., Y. H. Kim, and Y.-I. Won (2003), Observation of mesospheric waves with an all-sky camera in Korean Peninsula, *Adv. Space Res.*, *32*(5), 825–830.

Dewan, E. M., and R. H. Picard (1998), Mesospheric bores, *J. Geophys. Res.*, *103*(D6), 6295–6305.

Dewan, E. M., and R. H. Picard (2001), On the origin of mesospheric bores, *J. Geophys. Res.*, *106*(D3), 2921–2927.

Fritts, D. C. (2000), Errant inferences of gravity wave momentum and heat fluxes using airglow and lidar instrumentation: Corrections and cautions, *J. Geophys. Res.*, *105*(D17), 22,355–22,360.

Fritts, D. C., and L. Yuan (1989), An analysis of gravity wave ducting in the atmosphere: Eckart's resonances in thermal and Doppler ducts, *J. Geophys. Res.*, *94*(D15), 18,455–18,466.

Fukao, S., M. D. Yamanaka, J. Ao, W. K. Hocking, T. Sato, and M. Yamamoto (1994), Seasonal variability of vertical eddy diffusivity in the middle atmosphere 1. Three-year observations by the middle and upper atmosphere radar, *J. Geophys. Res.*, *99*(D9), 18,973–18,987.

Gossard, E. E., and W. H. Hooke (1975), *Waves in the Atmosphere*, Elsevier Sci., New York.

Hecht, J. H. (2004), Instability layers and airglow imaging, *Rev. Geophys.*, *42*, RG1001, doi:10.1029/2003RG000131.

Hecht, J. H., R. L. Walterscheid, M. P. Hickey, and S. J. Franke (2001), Climatology and modeling of quasi-monochromatic atmospheric gravity waves observed over Urbana, Illinois, *J. Geophys. Res.*, *106*(D6), 5181–5195.

Hedin, A. E. (1991), Extension of the MSIS thermospheric model into the middle and lower atmosphere, *J. Geophys. Res.*, *96*(A2), 1159–1172.

Hickey, M. P., and Y. Yu (2005), A full-wave investigation of the use of a "cancellation factor" in gravity wave-OH airglow interaction studies, *J. Geophys. Res.*, *110*, A01301, doi:10.1029/2003JA010372.

Hickey, M. P., R. L. Walterscheid, M. J. Taylor, W. Ward, G. Schubert, Q. Zhou, F. Garcia, M. C. Kelly, and G. G. Shepherd (1997), Numerical simulations of gravity waves imaged over Arecibo during the 10-day January 1993 campaign, *J. Geophys. Res.*, *102*(A6), 11,475–11,490, doi:10.1029/97JA00181.

Hines, C. O., and D. W. Tarasick (1987), On the detection and utilization of gravity waves in airglow studies, *Planet. Space Sci.*, *35*, 851–866.

Hines, C. O., and D. W. Tarasick (1994), Airglow response to vertically standing gravity waves, *Geophys. Res. Lett.*, *21*(24), 2729–2732.

Hocking, W. K. (1990), Turbulence in the region 80–120 km, *Adv. Space Res.*, *10*(12), 153–161.

Horinouchi, T. (2004), Simulated breaking of convectively generated mesoscale gravity waves and airglow modulation, *J. Atmos. Sol. Terr. Phys.*, *66*, 755–767.

Huang, T.-Y., and M. Hickey (2007), On the latitudinal variations of the non-periodic response of minor species induced by a dissipative gravity-wave packet in the MLT region, *J. Atmos. Sol. Terr. Phys.*, *69*(6), 741–757, doi:10.1016/j.jastp.2007.01.011.

Huang, T.-Y., M. Hickey, and T. F. Tuan (2003), On nonlinear response of minor species with a layered structure to gravity waves, *J. Geophys. Res.*, *108*(A5), 1173, doi:10.1029/2002JA009497.

Isler, J. R., M. J. Taylor, and D. C. Fritts (1997), Observational evidence of wave ducting and evanescence in the mesosphere, *J. Geophys. Res.*, *102*(D22), 26,301–26,313.

Krassovsky, V. I. (1972), Infrasonic variations of OH emission in the upper atmosphere, *Ann. Geophys.*, *28*, 739–746.

LeVeque, R. J. (2002), *Finite Volume Methods for Hyperbolic Problems*, Cambridge Univ. Press, New York.

Li, F., A. Z. Liu, and G. R. Swenson (2005), Characteristics of instabilities in the mesopause region over Maui, Hawaii, *J. Geophys. Res.*, *110*, D09S12, doi:10.1029/2004JD005097.

Liu, A. Z., and G. R. Swenson (2003), A modeling study of O_2 and OH airglow perturbations induced by atmospheric gravity waves, *J. Geophys. Res.*, *108*(D4), 4151, doi:10.1029/2002JD002474.

Makhlouf, U. B., R. H. Picard, and J. R. Winick (1995), Photochemical-dynamical modeling of the measured response of airglow to gravity waves 1. Basic model for OH airglow, *J. Geophys. Res.*, *100*(D6), 11,289–11,311.

Makhlouf, U. B., R. H. Picard, J. R. Winick, and T. F. Tuan (1998), A model for the response of the atomic oxygen 557.7 nm and the OH Meinel airglow to atmospheric gravity waves in a realistic atmosphere, *J. Geophys. Res.*, *103*(D6), 6261–6269.

McDade, I. C., D. P. Murtagh, R. G. H. Greer, P. H. G. Dickinson, G. Witt, J. Stegman, E. J. Llewellyn, L. Thomas, and D. B. Jenkins (1986), ETON 2: Quenching parameters for the proposed precursors of $O_2(b^1\Sigma_g^+)$ and $O(^1S)$ in the terrestrial nightglow, *Planet. Space Sci.*, *34*(9), 789–800.

McDade, I. C., E. J. Llewellyn, D. P. Murtagh, and R. G. H. Greer (1987), ETON 5: Simultaneous rocket measurements of the OH Meinel $\Delta v = 2$ sequence and (8,3) band emission profiles in the nightglow, *Planet. Space Sci.*, *35*(9), 1137–1147.

Meriwether, J. W. (1984), Ground based measurements of mesospheric temperatures by optical means, *Handb. MAP*, *13*, 1–18.

Murtagh, D. P., G. Witt, J. Stegman, I. C. McDade, E. J. Llewellyn, and F. Harris (1990), An assessment of proposed $O(^1S)$ and $O_2(b^1\Sigma_g^+)$ nightglow excitation parameters, *Planet. Space Sci.*, *38*(1), 43–53.

Nakamura, T., A. Higashikawa, T. Tsuda, and Y. Matsushita (1999), Seasonal variations of gravity wave structures in OH airglow with a CCD imager at Shigaraki, *Earth Planets Space*, *51*, 897–906.

Nicolaides, C., O. Sinanoğlu, and P. Westhaus (1971), Theory of atomic structure including electron correlation. IV. Method for forbidden-transition probabilities with results for [O I], [O II], [O III], [N I], [N II], and [C I], *Phys. Rev. A.*, *4*(4), 1400–1410.

Nielsen, K., M. J. Taylor, N. Mitchell, W. Singer, and R. A. Goldberg (2006a), Observations of short-period gravity waves during the MAC-Wave 2003 winter campaign, *Ann. Geophys.*, *24*, 1227–1243.

Nielsen, K., M. J. Taylor, R. G. Stockwell, and M. J. Jarvis (2006b), An unusual mesospheric bore event observed at high latitudes over antarctica, *Geophys. Res. Lett.*, *33*, L07803, doi:10.1029/2005GL025649.

Schubert, G., and R. L. Walterscheid (1988), Wave-driven fluctuations in OH nightglow from an extended source region, *J. Geophys. Res.*, *93*(A9), 9903–9915.

Schubert, G., R. L. Walterscheid, M. P. Hickey, and C. A. Tepley (1999), Observations and interpretation of gravity wave induced fluctuations in the O I (557.7 nm) airglow, *J. Geophys. Res.*, *104*(A7), 14,915–14,924, doi:10.1029/1999JA900096.

Simkhada, D. B., J. B. Snively, M. J. Taylor, and S. J. Franke (2009), Analysis and modeling of ducted and evanescent gravity waves observed in the Hawaiian airglow, *Ann. Geophys.*, *27*(8), 3,213–3,224.

Smith, A. K., D. R. Marsh, J. M. Russell, M. G. Mlynczak, F. J. Martin-Torres, and E. Kyrölä (2008), Satellite observations of high nighttime ozone at the equatorial mesopause, *J. Geophys. Res.*, *113*, D17312, doi:10.1029/2008JD010066.

Smith, S. M., M. J. Taylor, G. R. Swenson, C. Y. She, W. K. Hocking, J. Baumgardner, and M. Mendillo (2003), A multidiagnostic investigation of the mesospheric bore phenomena, *J. Geophys. Res.*, *108*(A2), 1083, doi:10.1029/2002JA009500.

Snively, J. B., and V. P. Pasko (2003), Breaking of thundestorm-generated gravity waves as a source of short-period ducted waves at mesopause altitudes, *Geophys. Res. Lett.*, *30*(24), 2254, doi:10.1029/2003GL018436.

Snively, J. B., and V. P. Pasko (2005), Antiphase OH and OI airglow emissions induced by a short-period ducted gravity wave, *Geophys. Res. Lett.*, *32*, L08808, doi:10.1029/2004GL022221.

Snively, J. B., and V. P. Pasko (2008), Excitation of ducted gravity waves in the lower thermosphere by tropospheric sources, *J. Geophys. Res.*, *113*, A06303, doi:10.1029/2007JA012693.

Snively, J. B., V. P. Pasko, M. J. Taylor, and W. K. Hocking (2007), Doppler ducting of short-period gravity waves by midlatitude tidal wind structure, *J. Geophys. Res.*, *112*, A03304, doi:10.1029/2006JA011895.

Sutherland, B. R., and K. Yewchuk (2004), Internal wave tunnelling, *J. Fluid Mech.*, *511*, 125–134.

Swenson, G. R., and C. S. Gardner (1998), Analytical models for the response of the mesospheric OH* and Na layers to atmospheric gravity waves, *J. Geophys. Res.*, *103*(D6), 6271–6294.

Swenson, G. R., M. J. Alexander, and R. Haque (2000), Dispersion imposed limits on atmospheric gravity waves in the mesosphere: Observations from OH airglow, *Geophys. Res. Lett.*, *27*(6), 875–878.

Tarasick, D. W., and G. G. Shepherd (1992), Effects of gravity waves on complex airglow chemistries, 2. OH emission, *J. Geophys. Res.*, *97*(A3), 3195–3208.

Taylor, M. J. (1997), A review of advances in imaging techniques for measuring short period gravity waves in the mesosphere and lower thermosphere, *Adv. Space Res.*, *19*, 667–676.

Taylor, M. J., D. N. Turnbull, and R. P. Lowe (1995), Spectrometric and imaging measurements of a spectacular gravity wave event observed during the ALOHA-93 campaign, *Geophys. Res. Lett.*, *22*(20), 2849–2852.

Taylor, M. J., W. R. Pendleton, S. Clark, H. Takahashi, D. Gobbi, and R. A. Goldberg (1997), Image measurements of short-period gravity waves at equatorial latitudes, *J. Geophys. Res.*, *102*(D22), 26,283–26,299.

Taylor, M. J., W. R. Pendleton, C. S. Gardner, and R. J. States (1999), Comparison of terdiurnal tidal oscillations in mesospheric OH rotational temperature and Na lidar temperature measurements at mid-latitudes for fall/spring conditions, *Earth Planets Space*, *51*, 877–885.

Turnbull, D. N., and R. P. Lowe (1989), New hydroxyl transition probabilities and their importance in airglow studies, *Planet. Space Sci.*, *37*(6), 723–738, doi:10.1016/0032-0633(89)90042-1.

Vadas, S. L., D. C. Fritts, and M. J. Alexander (2003), Mechanism for the generation of secondary waves in wave breaking regions, *J. Atmos. Sci.*, *60*, 194–214.

Vargas, F., G. R. Swenson, A. Z. Liu, and D. Gobbi (2007), $O(^1S)$, OH, and O_2 (b) airglow layer perturbations due to AGWs and their implied effects on the atmosphere, *J. Geophys. Res.*, *112*, D14102, doi:10.1029/2006JD007642.

Walterscheid, R. L., G. Schubert, and J. M. Straus (1987), A dynamical-chemical model of wave-driven fluctuations in the OH nightglow, *J. Geophys. Res.*, *92*(A2), 1241–1254.

Walterscheid, R. L., J. H. Hecht, R. A. Vincent, I. M. Reid, J. Woithe, and M. P. Hickey (1999), Analysis and interpretation of airglow and radar observations of quasi-monochromatic gravity waves in the upper mesosphere and lower thermosphere over Adelaide, Australia, *J. Atmos. Sol. Terr. Phys.*, *61*, 461–478.

Walterscheid, R. L., G. Schubert, and D. G. Brinkman (2001), Small-scale gravity waves in the upper mesosphere and lower thermosphere generated by deep tropical convection, *J. Geophys. Res.*, *106*(D23), 31,825–31,832.

Winick, J. R. (1983), Photochemical processes in the mesosphere and lower thermosphere, in *Solar-Terrestrial Physics: Principles and Theoretical Foundations*, edited by W. H. Matthaeus, pp. 677–732, D. Reidel, Dordrecht, Netherlands.

Xu, J., A. K. Smith, and G. P. Brasseur (2001), Conditions for the photochemical destabilization of gravity waves in the mesopause region, *J. Atmos. Sol. Terr. Phys.*, *63*(17), 1821–1829.

Yamada, Y., H. Fukunishi, T. Nakamura, and T. Tsuda (2001), Breaking of small-scale gravity wave and transition to turbulence observed in OH airglow, *Geophys. Res. Lett.*, *28*(11), 2153–2156.

Yu, Y., and M. P. Hickey (2007), Time-resolved ducting of atmospheric acoustic-gravity waves by analysis of the vertical energy flux, *Geophys. Res. Lett.*, *34*, L02821, doi:10.1029/2006GL028299.

Zhang, S. P., and G. G. Shepherd (1999), The influence of the diurnal tide on the $O(^1S)$ and OH emission rates observed by WINDII on UARS, *Geophys. Res. Lett.*, *26*(4), 529–532.

Zhao, Y., M. J. Taylor, and X. Chu (2005), Comparison of simultaneous Na lidar and mesospheric nightglow temperature measurements and the effects of tides on the emission layer height, *J. Geophys. Res.*, *110*, D09S07, doi:10.1029/2004JD005115.

V. P. Pasko, Communications and Space Sciences Laboratory, Department of Electrical Engineering, Pennsylvania State University, 211B Electrical Engineering East, University Park, PA 16802, USA. (vpasko@psu.edu)

J. B. Snively, Department of Physical Sciences, Embry-Riddle Aeronautical University, 600 S. Clyde Morris Blvd., Daytona Beach, FL 32114-3900, USA. (jonathan.snively@erau.edu)

M. J. Taylor, Center for Atmospheric and Space Sciences, Utah State University, 4405 Old Main Hill, Logan, UT 84321, USA. (mike.taylor@usu.edu)